Remarkable Thermochromism in the Double Perovskite Cs$_2$NaFeCl$_6$

Fuxiang Ji, Johan Klarbring, Bin Zhang, Feng Wang, Linqin Wang, Xiaohe Miao, Weihua Ning,* Muyi Zhang, Xinyi Cai, Babak Bakhit, Martin Magnuson, Xiaoming Ren, Licheng Sun, Mats Fahlman, Irina A. Buyanova, Weimin M. Chen, Sergei I. Simak, Igor A. Abrikosov,* and Feng Gao*

Lead-free halide double perovskites (HDPs) have emerged as a new generation of thermochromic materials. However, further materials development and mechanistic understanding are required. Here, a highly stable HDP Cs$_2$NaFeCl$_6$ single crystal is synthesized, and its remarkable and fully reversible thermochromism with a wide color variation from light-yellow to black over a temperature range of 10 to 423 K is investigated. First-principles, density functional theory (DFT)-based calculations indicate that the thermochromism in Cs$_2$NaFeCl$_6$ is an effect of electron–phonon coupling. The temperature sensitivity of the bandgap in Cs$_2$NaFeCl$_6$ is up to 2.52 meVK^{-1} based on the Varshni equation, which is significantly higher than that of lead halide perovskites and many conventional group-IV, III–V semiconductors. Meanwhile, this material shows excellent environmental, thermal, and thermochromic cycle stability. This work provides valuable insights into HDPs' thermochromism and sheds new light on developing efficient thermochromic materials.

1. Introduction

Lead halide perovskites have shown interesting stimuli-responsive properties due to their low formation energy and soft crystal nature.[1–4] By exposure to external stimuli such as temperature, pressure, electric field, and chemical environment, halide perovskites readily undergo reversible chemical and structural transformation, which switches their optical and electrical properties.[5] Among various external stimuli, temperature represents a fundamental and readily controllable one that has garnered growing interest. Temperature-induced switchable optical properties change in materials, also known as thermochromism, is valuable for a range of important applications, including smart windows, temperature sensors, vision thermometers, and other on-demand devices.[6–9] Notably, lead halide perovskites with the perovskite phase (3D perovskite structure) usually exhibit weak temperature-dependent optical property changes. Taking the benchmark lead-based perovskite CH$_3$NH$_3$PbI$_3$ (MAPbI$_3$) as an example, the absorption edge only slightly blueshifts from ≈770 to ≈734 nm as the temperature increases from 293 to 400 K.[10] Thus, utilizing

F. Ji, J. Klarbring, B. Zhang, F. Wang, W. Ning, M. Zhang, X. Cai, B. Bakhit, M. Magnuson, I. A. Buyanova, W. M. Chen, S. I. Simak, I. A. Abrikosov, F. Gao
Department of Physics, Chemistry and Biology (IFM)
Linköping University
Linköping SE-581 83, Sweden
E-mail: whning@suda.edu.cn; igor.abrikosov@liu.se; feng.gao@liu.se
L. Wang, L. Sun
Center of Artificial Photosynthesis for Solar Fuels, School of Science
Westlake University
Hangzhou 310024, P.R. China

X. Miao
Instrumentation and Service Center for Physical Sciences
Westlake University
Hangzhou 310024, P.R. China

W. Ning
Jiangsu Key Laboratory of Advanced Negative Carbon Technologies, Institute of Functional Nano and Soft Materials (FUNSOM)
Soochow University
Suzhou 215123, P. R. China

X. Ren
State Key Laboratory of Materials-Oriented Chemical Engineering and College of Chemistry and Molecular Engineering
Nanjing Tech University
Nanjing 210009, P. R. China

M. Fahlman
Department of Science and Technology
Linköping University
Norrköping 60174, Sweden

S. I. Simak
Department of Physics and Astronomy
Uppsala University
Uppsala SE-75120, Sweden

**ADVANCED
SCIENCE NEWS**

www.advancedsciencenews.com

**ADVANCED
OPTICAL
MATERIALS**

www.advopticalmat.de
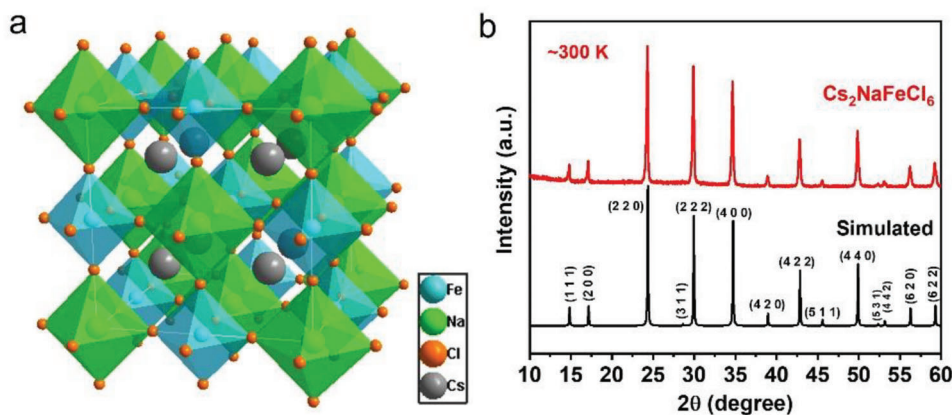
Figure 1. a) Crystal structure of the ordered double perovskite $Cs_2NaFeCl_6$. Blue, green, origin, and grey spheres represent Fe, Na, Cl, and Cs atoms, respectively. b) PXRD patterns of $Cs_2NaFeCl_6$ powder. The simulated XRD of $Cs_2NaFeCl_6$ is obtained from Mercury software simulation.

temperature-induced phase transitions between the perovskite phase and a non-perovskite phase has become the major approach to exploit the thermochromism in lead halide perovskites.[9,11–13] For instance, an obvious and reversible thermochromic behavior in $CH_3NH_3PbI_3$ was explored through the temperature-dependent dehydration/hydration process between the $CH_3NH_3PbI_3$ and $(CH_3NH_3)_4PbI_6\cdot2H_2O$ phases.[11] Using CH_3NH_2 gas to switch the transparent $CH_3NH_3PbI_3\bullet xCH_3NH_2$ intermedial phase and $CH_3NH_3PbI_3$ perovskite phase upon photothermal heating/cooling can also induce reversible thermochromism.[12] Afterward, Yang and co-workers developed a smart photovoltaic window through the temperature-induced phase transitions between a transparent non-perovskite phase and a deeply colored perovskite phase in the mixed-halide perovskite $CsPbI_{3-x}Br_x$.[13] However, reversible phase transitions usually require several and complicated stimuli environments, resulting in long response times (even several hours) and poor cycle stability. Besides, the toxicity of lead and the intrinsic thermal instability of lead halide perovskites[14] further limit their practical application in thermochromism.

To address these bottlenecks of lead halide perovskites, one of the most promising approaches is to replace them with HDPs.[15,16] HDPs have superior thermal stability, no or low toxicity, and a large pool of candidates by combining different metal ions,[15–20] but the exploration of their thermochromism is still in its infancy. Recently, we reported the fully reversible thermochromism in the benchmark HDP $Cs_2AgBiBr_6$ for the first time, which exhibits a short response time (several seconds) and excellent cycle stability.[21] The main drawback is its narrow absorption variation of around 20 nm between 300 and 523 K, which is unsatisfactory for potential thermochromic applications. The mechanism behind the thermochromism in $Cs_2AgBiBr_6$ was further revealed by our DFT calculations, primarily related to the combined effects of temperature-induced structural changes, spin-orbit coupling effect, and electron–phonon coupling, without phase transitions.[21] In light of these findings, further enhancing these effects by modifying the host material or exploring other new compositions could potentially improve thermochromism properties. Meanwhile, more efforts are still required to further refine and gain insight into the fundamental mechanism of thermochromism in HDPs, which is crucial for
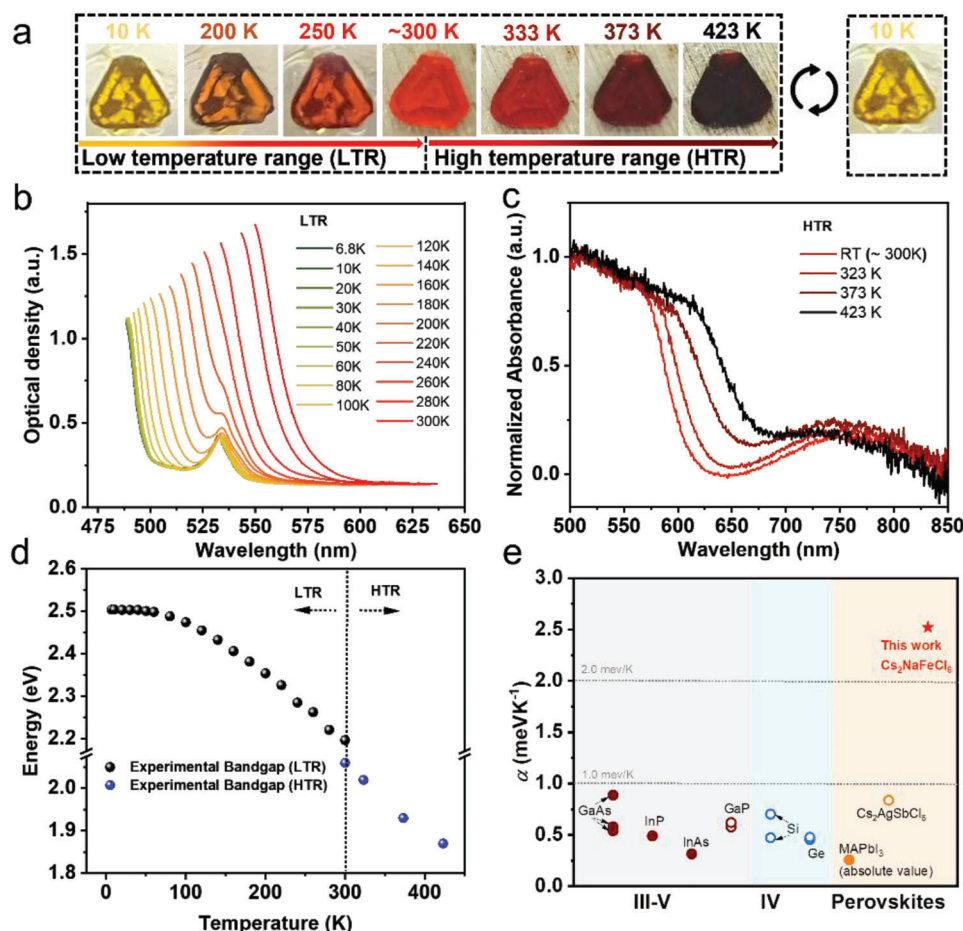
tailoring and designing suitable candidates to realize their full potential.

Here, we choose $Cs_2NaFeCl_6$ with strong electron-phonon coupling as the target material and explore its reversible thermochromism. Impressively, compared with the benchmark HDP $Cs_2AgBiBr_6$, $Cs_2NaFeCl_6$ shows much broader optical bandgap changes of 0.51 eV between 10 and 423 K. Temperature-dependent XRD data indicate reversible lattice expansion and contraction during heating/cooling cycles. Based on this structural behavior, we perform DFT calculations to demonstrate that the thermochromism results from an effect of strong electron–phonon coupling in $Cs_2NaFeCl_6$.

2. Results and Discussion

High-quality $Cs_2NaFeCl_6$ single crystals were synthesized from HCl acid containing stoichiometric CsCl, NaCl, and $FeCl_3$ by the hydrothermal method (more details are shown in the experimental section). Single-crystal X-ray diffraction (SCXRD) data show that $Cs_2NaFeCl_6$ crystallizes in the cubic system with a space group of $Fm\bar{3}m$ (Table S1, Supporting Information). Specifically, the $[NaCl_6]^{5-}$ and $[FeCl_6]^{3-}$ octahedra are corner connected, and the Cs^+ cations are located in the cavities formed by the octahedra, as shown in **Figure 1**a. The powder X-ray diffraction (PXRD) pattern of $Cs_2NaFeCl_6$ shows identical features as the simulated spectra based on the single crystal structure (Figure 1b), indicating high phase-purity. The high purity is further confirmed by the energy dispersive spectroscopy (EDS) result in Figure S1 (Supporting Information).

We explore the temperature-dependent optical properties of $Cs_2NaFeCl_6$ single crystals to evaluate their thermochromic applications. The $Cs_2NaFeCl_6$ single crystal exhibits rich thermochromic behavior with the crystal color changing gradually from light yellow to black in the range of 10–423 K, as shown in **Figure 2**a. It is worth noting that the temperature-induced color transition is fully reversible; the crystal color turns back to its original color as the temperature cools down. To quantify the color changes, we perform the Ultraviolet-Visible (UV–vis) measurements on the $Cs_2NaFeCl_6$ crystal at different temperatures. Experimentally, we employ two different modes of measurements, namely transmittance and reflectance, to examine the

ADVANCED
SCIENCE NEWS
www.advancedsciencenews.com

ADVANCED
OPTICAL
MATERIALS
www.advopticalmat.de

Figure 2. a) Optical images of $Cs_2NaFeCl_6$ single crystal at different temperatures. UV–vis absorption spectra of $Cs_2NaFeCl_6$ single crystal at b) low-temperature range (LTR) and c) high-temperature range (HTR). d) Plots of the optical bandgap of $Cs_2NaFeCl_6$ as a function of temperature. e) Comparison of the temperature-induced bandgap change rate (fitting parameter α through Varshni equation) for various group IV, III–V semiconductors, and perovskites. The spheres and circles represent direct and indirect bandgap, respectively. An absolute value is used for $MAPbI_3$. The data in the figure were extracted from below references.[10,22–24]

optical change of the $Cs_2NaFeCl_6$ crystals in the low-temperature range (LTR) (6.8 to 300 K) and high-temperature range (HTR) (≈300 (room temperature, RT) to 423 K), respectively. Carrying out these two different modes of measurements is primarily due to instrumental limitations. The transmittance and reflectance spectra of $Cs_2NaFeCl_6$, shown in Figure S2 (Supporting Information), are converted to absorbance spectra in Figure 2b,c. In the LTR of 6.8 to 300 K, the absorption edge gradually shifts from ≈495 to ≈565 nm (Figure 2b). As the temperature further increases from RT (≈300 K) to 473 K, the absorption edge further gradually redshifts to ≈663 nm (Figure 2c), corresponding well with the observed crystal color changes.

By extrapolating the linear region in the Tauc plot of absorption to the energy–axis intercept, we determine the optical direct bandgaps of the $Cs_2NaFeCl_6$ crystals at different temperatures (Figure S3, Supporting Information). We note the characteristic weakly temperature-dependent behavior of the optical bandgap at the very low-temperature range from ≈6.8 to 80 K, followed by a rather steep decrease with temperature (Figure 2d). Specifically, the optical bandgap of $Cs_2NaFeCl_6$ is reduced from 2.50 to

2.19 eV when the temperature increases from 6.8 to 300 K, and further decreased from 2.06 to 1.87 eV by increasing the temperature from RT (≈300 K) to 423 K. We also find a discrepancy between the optical bandgap at ≈300K calculated from transmittance and reflectance results, which is mainly related to the unfavorable background in the reflectance spectra that is challenging to remove experimentally, and the different crystal thickness employed for these two different measurement modes. Specifically, a thin crystal (≈0.75 mm) is used to measure transmittance, whereas a thick crystal (≈1.3 mm) is used to measure diffuse reflectance.

To show the thermochromic behavior in $Cs_2NaFeCl_6$ more clearly, we further plot the bandgap difference compared to the bandgap at 300 K as a function of temperatures in Figure S4 (Supporting Information), where the temperature-induced bandgap change from 6.8 to 423 K is as high as 0.51 eV. In general, the temperature-induced bandgap change of semiconductors is well described by the Varshni relation.[22]

$$\Delta E_g(T) = \Delta E_g(0) - \frac{\alpha T^2}{\beta + T} \qquad (1)$$
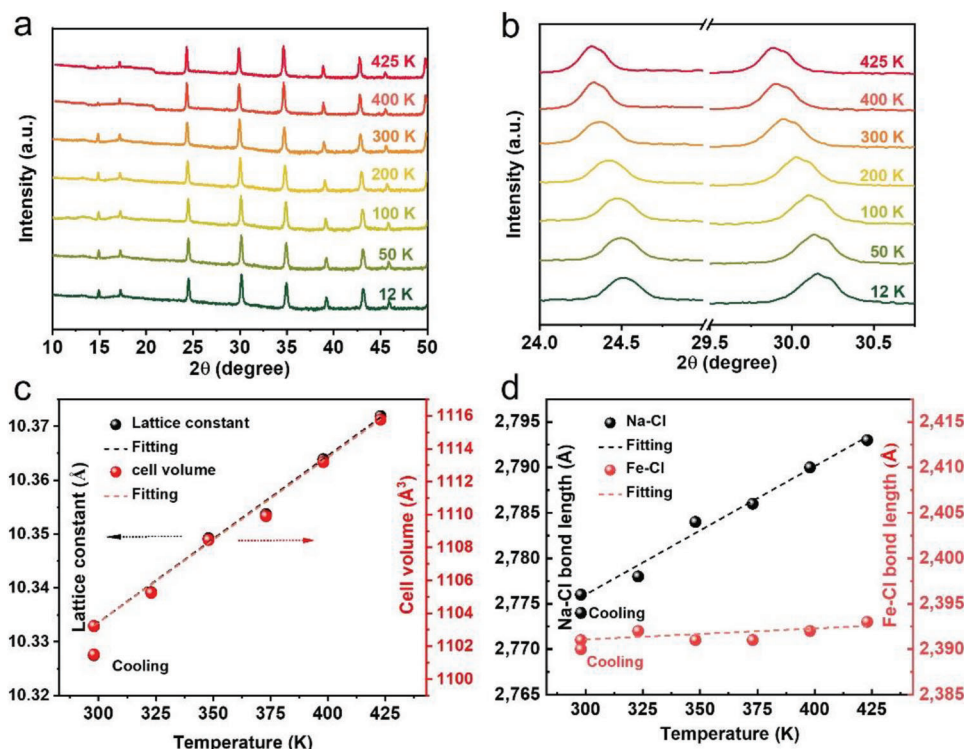
Figure 3. a) Temperature-dependent PXRD patterns of $Cs_2NaFeCl_6$. b) An enlarged view of reflections (220) and (222) in the temperature-dependent PXRD patterns. c) Temperature-dependent lattice constant and cell volume V of $Cs_2NaFeCl_6$ single crystal in the 298–423 K temperature range. d) Variation of Na—Cl and Fe—Cl bond lengths in the temperature range of 298–423 K. Cooling means the crystal returns to room temperature after one heating/cooling cycle (from 298 to 423 to 298 K).

where α and β are fitting parameters for a given material. Notably, the bandgap of the $Cs_2NaFeCl_6$ shows a remarkable temperature sensitivity with $\alpha = 2.52$ meVK^{-1}, which is dramatically larger than that of lead halide perovskites and many conventional group-IV, III-V semiconductors,[10,22–24] including Si (0.7021 meVK^{-1}; 0.4730 meVK^{-1}), Ge (0.4561 meVK^{-1}; 0.4774 meVK^{-1}), GaAs (0.8871 meVK^{-1}; 0.58 meVK^{-1}; 0.5405 meVK^{-1}), InAs (0.3158 meVK^{-1}), InP (0.4906 meVK^{-1}), GaP (0.5771 meVK^{-1}; 0.62 meVK^{-1}), $Cs_2AgSbCl_6$ (0.837 meVK^{-1}), and $MAPbI_3$ (−0.257 meVK^{-1}), as shown in Figure 2e. It should be noted that lead-based perovskites, including $MAPbI_3$, exhibit an opposite behavior to $Cs_2NaFeCl_6$ and these conventional group-IV, III-V semiconductors, as their bandgap continuously increases with rising temperature.

To seek further insight into the nature of the thermochromic behavior in $Cs_2NaFeCl_6$, we investigate the temperature evolution of its structure. We first perform temperature-dependent PXRD from 12 to 425 K, as shown in **Figure 3**a. The main change of the PXRD patterns is that all the diffraction peaks (e.g., 220, 222, etc.) shift toward a lower angle with increasing temperature, indicating the lattice expansion during heating (Figure 3b). In addition, the diffraction peaks are fully recoverable after one heating/cooling cycle, which indicates that the process is completely reversible (Figure S5, Supporting Information). Interestingly, the temperature-dependent PXRD behavior is similar to that of the optical bandgap, with a very slow peak shift below 100 K followed by a rapid shift above 100 K. Considering the

more pronounced structural changes in the HTR, we perform temperature-dependent SCXRD measurements to further confirm the evolution of the crystal structure between 298 and 423 K (Table S1, Supporting Information). We extract the cell parameters and volumes of $Cs_2NaFeCl_6$ double perovskite at different temperatures based on the SCXRD results, as shown in Figure 3c. A linear increase of the volume from 298 to 423 K indicates a thermal-induced lattice expansion without any phase transition, which is in agreement with the PXRD results. As expected, the volume of $Cs_2NaFeCl_6$ returns to approximately its original value after cooling to 298 K, confirming the reversibility of the thermochromism process.

We further analyze the Na/Fe—Cl bond length changes under various temperatures. It is noted that temperature-induced Na—Cl and Fe—Cl bond length change behavior is significantly different. The length of the longer Na—Cl bond significantly increases from 2.776 Å at 298 K to 2.793 Å at 423 K, while the length of the shorter Fe—Cl bond remains almost intact by increasing temperature (see Figure 3d). This behavior is reproduced in our DFT calculations. We perform a set of ab-initio molecular dynamics (AIMD) simulations at temperatures from 200 to 500 K, using the experimentally determined temperature-dependent lattice parameters, from which we extract the Na—Cl and Fe—Cl projected bond lengths. In agreement with our experimental results in Figure 3d, the AIMD calculations also show a sharp linear increase in the Na—Cl bond length as a function of temperature, while a slight increase in the length of Fe—Cl bond (**Figure 4**a). This difference in the temperature evolution
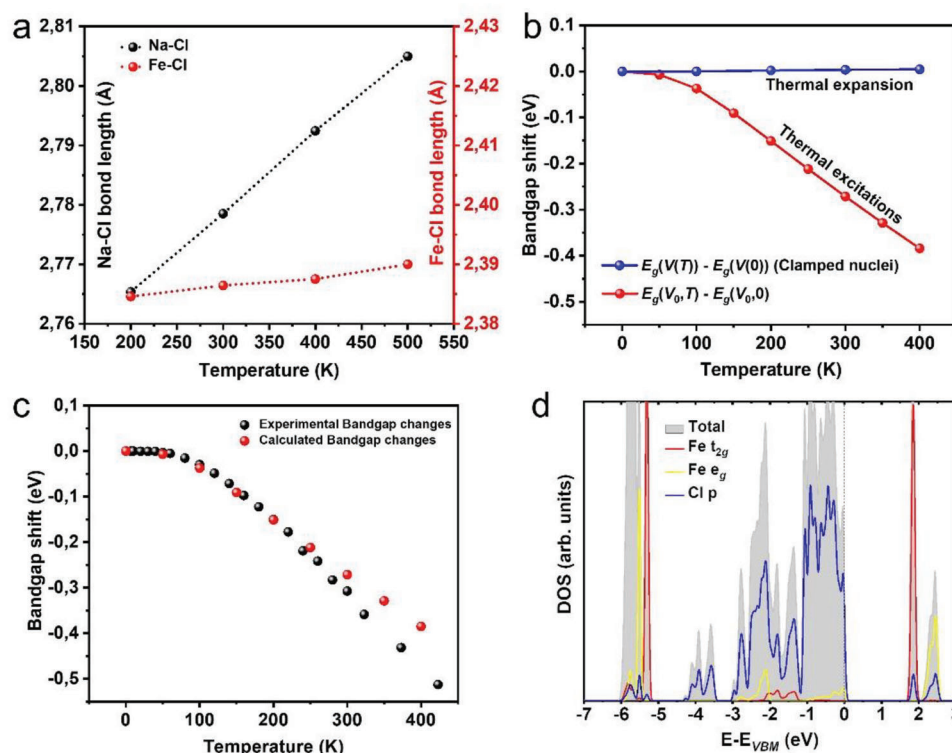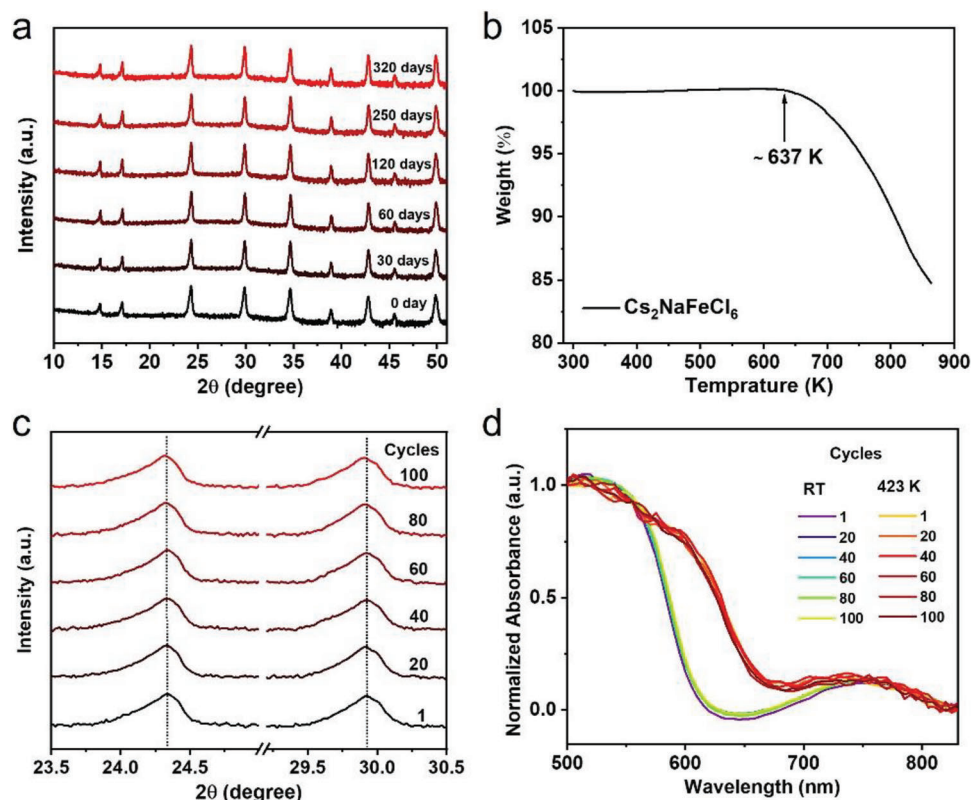
Figure 4. a) Fe—Cl and Na—Cl bond lengths extracted from AIMD simulations. b) Bandgap shift as a function of temperature, where temperature is treated only through thermal expansion (blue dots) and only through thermal excitations (red dots), see methods section for details. c) Comparison of the calculated and experimental bandgap shift of $Cs_2NaFeCl_6$ as a function of temperatures. d) Electronic DOS of $Cs_2NaFeCl_6$ calculated in the paramagnetic state.[33] E_{VBM} stands for the energy of the valence band maximum.

of the bond-lengths can be understood from the different nature of the Na—Cl and Fe—Cl bonds. While the Na—Cl bond is ionic in nature, the Fe—Cl bond is substantially covalent and much stronger. Thus, this results in a lattice expansion by primarily elongating the weaker Na—Cl bonds (Figure S6, Supporting Information). These changes are significantly different from those of the prototypical HDP $Cs_2AgBiBr_6$, where the bond lengths of Ag—Br and Bi—Br tend toward equal values on heating.[21]

Focusing on this structure and bonding behavior yields insights into the thermochromic mechanism of this system. Considering that both thermal expansion and thermal excitation (electron–phonon coupling) occur with heating, we perform first-principles calculations on the temperature shifts of the bandgap of $Cs_2NaFeCl_6$ in two cases (Figure 4b). First, we only consider thermal expansion, i.e., all atoms are clamped at their relaxed positions, but the volume is expanded following the experimentally determined temperature dependent volume. Full atomic relaxation is performed at each volume, which as mentioned above, it changes the Fe—Cl bond length very little. We see that the resulting change of the bandgap is very small. Second, we show the bandgap shift on including the effect of thermal excitations, i.e., electron–phonon coupling (using the real space single-shot "special displacement" approach),[25] where we observe a large shift in the bandgap. This indicates, first, that the thermochromism in $Cs_2NaFeCl_6$ does not appear to be driven by thermal expansion. Second, it suggests that a change in the Fe—Cl bonding

environment is necessary to induce a change in the bandgap. Although theoretically, the contribution of thermal expansion to the thermochromism in $Cs_2NaFeCl_6$ is negligible, further experimental evidence is still required to substantiate this claim in the future. For instance, pressure-dependent UV–vis measurements could be employed to determine the pressure coefficient of its bandgap.[26]

To further verify the accuracy, we compare the DFT-calculated temperature-dependent electronic bandgap shift with the measured optical bandgap shift in Figure 4c. Notably, we find good agreement, suggesting that the thermochromism of $Cs_2NaFeCl_6$ could be described as an effect of strong electron–phonon coupling effect on the bandgap and does not require any Na/Fe order-disorder mechanism, as was previously proposed.[27] This good agreement also implies a negligible explicit effect of thermal expansion on the thermochromism of $Cs_2NaFeCl_6$. However, future studies analyzing its high-pressure dependent bandgap data are still necessary to experimentally confirm this claim. It is important to note that achieving a quantitative convergence of the effect of electron–phonon coupling on the bandgap with respect to the supercell size is likely prohibitively computationally expensive.[28] Furthermore, polaronic and non-adiabatic effects, which are not included in our calculations, could potentially be important. Nevertheless, the good agreement with our experimental measurements indicates that we do capture the correct temperature dependence of the bandgap. Furthermore, it is clear that the electron-phonon coupling of $Cs_2NaFeCl_6$ is very

**ADVANCED
SCIENCE NEWS**
www.advancedsciencenews.com

**ADVANCED
OPTICAL
MATERIALS**
www.advopticalmat.de

Figure 5. a) Time-dependent PXRD patterns of $Cs_2NaFeCl_6$ powder after exposure to ambient atmosphere. b) Thermogravimetric curve of $Cs_2NaFeCl_6$ powder. c) The enlarged view of the (220) and (222) diffraction peaks of $Cs_2NaFeCl_6$ powder for repeating 100 heating/cooling cycles between RT and 423 K. d) Normalized temperature-dependent UV–vis absorption spectra of $Cs_2NaFeCl_6$ single crystal for repeating 100 heating/cooling cycles between RT and 423 K.

strong, as can be quantified by the large calculated zero-point renormalization (ZPR) of the bandgap of ≈ 0.34 eV. Indeed, this value is significantly larger than those of many "conventional" semiconductors with similar average atomic mass (or similar average phonon frequency) as $Cs_2NaFeCl_6$, such as Ge (0.049 eV), GaAs (0.056 eV), CdTe (0.015 eV), etc.[29] Our recent work also confirms the strong electron–phonon coupling in $Cs_2NaFeCl_6$ by temperature-dependent Raman measurements.[30] These findings may explain its significantly higher temperature sensitivity of bandgap (α value) than many conventional semiconductors.

The fact that a change in the Fe—Cl bonding environment is needed to induce a change in the bandgap is not surprising, considering the ion-clamped electronic density of states (DOS) in Figure 4d. Indeed, both the valence and conduction band edges are made up of Fe(d)—Cl(p) hybridized states. This is shown experimentally by valence band X-ray photoelectron spectroscopy (XPS) in Figure S10 (Supporting Information). In particular, the highly localized and directional nature of the Fe(d) states at the conduction band edge should be sensitive to thermal excitations that distort the octahedral Fe—Cl bonding environment, similar to what was reported for $Cs_2AgInCl_6$ in Ref.[31] Interestingly, the structurally and chemically related material Cs_2NaScF_6 was recently identified as an outlier in terms of large ZPR in a computational high-throughput study,[32] perhaps indicating that the double-perovskite structure with a conduction band of localized

d-states is generally susceptible to strong renormalization of the bandgap by electron–phonon coupling.

Stability is an important parameter to evaluate the potential long-term use of HDPs for thermochromic applications. We investigate the environmental and thermal stability of $Cs_2NaFeCl_6$ by time-dependent PXRD and thermogravimetric measurements. **Figure 5**a shows the time-dependent PXRD of $Cs_2NaFeCl_6$, demonstrating its excellent environmental stability as indicated by negligible decomposition of the sample after being stored in the air (30–60% humidity) for 320 days. Thermogravimetric analysis (TGA) measurements indicate that $Cs_2NaFeCl_6$ possesses high thermal stability, with a decomposition temperature above 637 K (Figure 5b). As the more obvious optical bandgap variation in the HTR is more promising for practical application, cycle stability is further investigated. Impressively, the $Cs_2NaFeCl_6$ exhibits excellent thermochromic cycle stability without crystal color changes after repeating 100 heating/cooling cycles in the HTR (Figure S7, Supporting Information). This can be further confirmed by the cycle-dependent PXRD patterns (Figure 5c; Figure S8, Supporting Information) and UV–vis diffuse reflectance spectra (Figure 5d; Figure S9, Supporting Information), which show negligible changes after heating/cooling cycles. This excellent thermochromic cycle stability in the $Cs_2NaFeCl_6$ at HTR is possibly related to the fact that only lattice expansion occurs in the crystal during heating/cooling without phase transition.

**ADVANCED
SCIENCE NEWS**

www.advancedsciencenews.com

**ADVANCED
OPTICAL
MATERIALS**

www.advopticalmat.de

3. Conclusion

In summary, we investigated the remarkable and fully reversible thermochromic behavior in double perovskite $Cs_2NaFeCl_6$. Attractively, the temperature sensitivity of the bandgap of $Cs_2NaFeCl_6$ crystal is as high as 2.52 meVK^{-1} and the bandgap change from 6.8 to 423 K is 0.51 eV, significantly exceeding the values reported in lead-based perovskites and many conventional group-IV and III–V semiconductors. We show a very good agreement between the measured and first-principles calculated bandgaps in $Cs_2NaFeCl_6$. The first-principles calculations indicate that the dramatic thermochromism in $Cs_2NaFeCl_6$ is attributed to a strong electron–phonon coupling. Specifically, the conduction band edge contains Fe(d) states that are highly localized and directional, making them particularly sensitive to thermal excitations that change the Fe—Cl bonding environment. Furthermore, the theoretically suggested negligible explicit contribution of thermal expansion in the thermochromism of $Cs_2NaFeCl_6$ still calls for future experimental validation under high-pressure conditions. The environmentally stable $Cs_2NaFeCl_6$ crystals show excellent thermochromic cycle stability without property changes after repeating 100 heating/cooling cycles between RT and 423 K, making it a promising candidate for temperature sensors, visual thermometers, and other thermochromism applications. Furthermore, our finding highlights the great potential for exploiting thermochromism in lead-free perovskites.

4. Experimental Section

Materials Synthesis: All the chemicals used were purchased from Sigma–Aldrich without any further purification. For $Cs_2NaFeCl_6$ single crystals, solid CsCl (168.36 mg, 1.00 mmol), NaCl (29.22 mg, 0.5 mmol), and FeCl$_3$ (81.1 mg, 0.5 mmol) were dissolved in 7 mL of 37% HCl and then transferred into a 25 cm^3 Teflon-lined autoclave. The autoclave was sealed and placed in the oven, where it was heated to 180 °C for 12 h. After being slowly cooled to room temperature at a 1 °C h^{-1} rate, red $Cs_2NaFeCl_6$ single crystals were achieved.

Physical Measurements: The XRD patterns of the powders and thin films were recorded with a X'Pert PRO X-ray diffractometer using Cu Kα1 irradiation ($\lambda = 1.5406$ Å). Variable-temperature PXRD data were collected using a Bruker D8 Discover with a high-brilliance rotational Cu anode (6 kW TXS-HE X-ray source) in the temperature range of 12–425 K by using Phenix cryostat and MTC furnace temperature chambers. The powders were obtained by single crystal grinding. Variable-temperature UV–vis spectroscopy in the high-temperature range ($\approx$300 (RT) to 423 K) was measured on a single crystal with a PerkinElmer Lambda 900 in diffuse reflectance mode. The in situ heating module in the UV–vis spectrophotometer was homemade using a laboratory hot plate. For low temperature transmission measurement, the sample was mounted in variable temperature He-flow cryostat. A Xenon lamp was employed as a light source and the transmitted signal light was analyzed by a grating monochromator equipped with a photomultiplier. Thermogravimetric (TG) experiments were performed with a STA449 F3 thermogravimetric analyzer in the range of 303–873 K at a warming rate of 20 K min^{-1} under a nitrogen atmosphere. The XPS measurements of the valence band of the double perovskite $Cs_2NaFeCl_6$ were performed in an Axis Ultra DLD instrument from Kratos Analytical (UK), employing monochromatic Al Kα radiation (hn = 1486.6 eV) and operated at a base pressure <1.1 × 10^{-9} Torr (1.5 × 10^{-7} Pa) during the data acquisition. The binding energy (BE) scale was calibrated using the ISO-certified procedure, with the spectra referenced to the Fermi edge in order to circumvent discrepancies associated with employing the C 1s peak from adventitious carbon.[34]

X-Ray Single Crystallography: The single-crystal X-ray diffraction (SXRD) data for $Cs_2NaFeCl_6$ were collected at 298, 323, 348, 373, 398, 423, and 298 K (cool down) with graphite monochromated Mo Kα ($\lambda = 0.71073$ Å) on a CCD area detector (Bruker-SMART), respectively. Data reductions and absorption corrections were performed with the SAINT and SADABS software packages, respectively. Structures were solved by a direct method using the SHELXL-97 software package.[35] The non-hydrogen atoms were anisotropically refined using the full-matrix least-squares method on F2. The details about data collection, structure refinement, and crystallography are summarized in Table S1 (Supporting Information).

Optical Bandgap Determination: The obtained reflectance spectra were converted to pseudo-absorbance spectra using the Kubelka–Munk transform.[36]

$$\alpha \approx (1 - R)^2 / 2R \tag{2}$$

where α = pseudo-absorbance and R = reflectance.

The transmittance (T) spectra were converted to absorbance spectra using the below equation.

$$\alpha \propto -\log_{10} T \tag{3}$$

Finally, the direct bandgaps were calculated by taking the intercept upon extrapolation of the linear regions of $(\alpha h\nu)^2$ versus E(eV).

First-Principles Calculations: The Density Functional Theory (DFT) calculations were performed in the framework of the Projector Augmented Wave (PAW) method[37] as implemented in the Vienna ab initio Simulation Package (VASP).[38–40] The PBEsol[41] form of the exchange correlation functional was used with an effective Hubbard U correction U_{eff} = 3 eV, in the scheme according to Dudarev et al.,[42] added to the Fe d states. Indeed, it was shown in Ref. [33] that using a value of U_{eff} = 3 eV provides consistent results between hybrid-DFT and DFT+U calculations.

The electron–phonon coupling calculations were performed using the real space "special-displacement" method,[25] as it is implemented in VASP.[29] In this method, calculated phonon frequencies and eigenvectors were used to generate one single set of displaced atomic positions in a supercell, optimally representing the thermally excited state of the system at a chosen temperature. Standard DFT calculations of the electronic structure are then performed on these thermally excited supercells. The phonon frequencies and eigenvectors needed to obtain the thermally excited supercells were obtained using VASP's finite-displacement phonon routines, with a displacement distance of 0.01 Å. A 4 × 4 × 4 expansion of the primitive face-centered cubic (fcc) supercell was used, containing 640 atoms, for these calculations. As pointed out in the main text, this supercell size might not be large enough to achieve quantitative converge of the effect of electron–phonon coupling on the electronic structure of $Cs_2NaFeCl_6$. Nevertheless, the temperature dependence of the bandgap was expected to be qualitatively correct.

A fixed lattice parameter of 10.27 Å was used for the electron–phonon coupling calculations. When modelling thermal expansion effects (Figure 4a,b), a lattice parameter of 10.27 Å was used for temperatures up to 100 K and then follow the experimentally determined thermal expansion for higher temperatures.

$Cs_2NaFeCl_6$ was paramagnetic above $\approx$3 K,[43] and this disordered magnetic state was modeled using a disordered local moment (DLM) approach[44,45] that entailed distributing up and down spins on the Fe atoms in a special quasirandom structure (SQS) sense.[46] The phonon calculations were performed assuming a FM ordering of the Fe^{3+} magnetic moments, and this study made explicit tests that the magnetic state should have a small influence on the phonon dispersion. For the evaluation of the bandgaps in the thermally excited supercells the difference between the lowest unoccupied and highest occupied Kohn–Sham eigenvalues was extracted in both spin-channels separately and then use their average value. In principle one might want to average over all eigenvalues in the thermally excited supercells that were degenerate in the ion-clamped structure, but this was difficult in the present case both because of the many bands with energies close to the band edges and due to the

**ADVANCED
SCIENCE NEWS**

www.advancedsciencenews.com

**ADVANCED
OPTICAL
MATERIALS**

www.advopticalmat.de

symmetry breaking of from the magnetic disorder. Thus, the mentioned difference between the lowest unoccupied and highest occupied eigenvalues was simply used.

The kinetic energy cut off for the plane wave expansion of the Kohn–Sham orbitals was set to 620 eV for the phonon calculations and at least 400 eV for the rest, while the convergence criteria for the electronic iterations was set to 10^{-8} eV for phonon calculations and 10^{-5} eV for other calculations. A Gaussian smearing with a width of 0.05 eV was applied. The AIMD simulations were performed in the 320 atom supercell with a DLM magnetic state. A 2 fs timestep was used and the temperature was controlled using a Nosé-Hover thermostat, with the default Nosé mass as set by VASP. The production AIMD simulation runs started from structures equilibrated using cheaper AIMD settings and were then run for ≈ 14 ps, from which an additional 2 ps were skipped as equilibration time. The Brillouin Zone (BZ) of both the 320 atom supercells used in the AIMD and the 640 atom supercell used in the electron–phonon calculations were sampled at the Γ-point. Internal coordinates were relaxed until all forces were $<10^{-4}$ eV Å^{-1} for the phonon calculations. PAW potentials treating the Cs (5s5p6s), Na (2p3s), Fe (3d4s), and Cl (3s3p) states as valence were used.

[1] G. P. Nagabhushana, R. Shivaramaiah, A. Navrotsky, *Proc. Natl. Acad. Sci. USA* **2016**, *113*, 7717.

[2] D. T. Moore, H. Sai, K. W. Tan, D.-M. Smilgies, W. Zhang, H. J. Snaith, U. Wiesner, L. A. Estroff, *J. Am. Chem. Soc.* **2015**, *137*, 2350.

[3] J. Even, M. Carignano, C. Katan, *Nanoscale* **2016**, *8*, 6222.

[4] D. H. Fabini, T. Hogan, H. A. Evans, C. C. Stoumpos, M. G. Kanatzidis, R. Seshadri, *J. Phys. Chem. Lett.* **2016**, *7*, 376.

[5] A. A. Zhumekenov, M. I. Saidaminov, O. F. Mohammed, O. M. Bakr, *Joule* **2021**, *5*, 2027.

[6] Y. Ke, C. Zhou, Y. Zhou, S. Wang, S. H. Chan, Y. Long, *Adv. Funct. Mater.* **2018**, *28*, 1800113.

[7] W. Zhang, Z. Sun, J. Zhang, S. Han, C. Ji, L. Li, M. Hong, J. Luo, *J. Mater. Chem. C* **2017**, *5*, 9967.

[8] Y. Cui, Y. Ke, C. Liu, Z. Chen, N. Wang, L. Zhang, Y. Zhou, S. Wang, Y. Gao, Y. Long, *Joule* **2018**, *2*, 1707.

[9] Y. Zhang, C. Y. Tso, J. S. Iñigo, S. Liu, H. Miyazaki, C. Y. H. Chao, K. M. Yu, *Appl. Energy* **2019**, *254*, 113690.

[10] C. Quarti, E. Mosconi, J. M. Ball, V. D'Innocenzo, C. Tao, S. Pathak, H. J. Snaith, A. Petrozza, F. De Angelis, *Energy Environ. Sci.* **2016**, *9*, 155.

[11] A. Halder, D. Choudhury, S. Ghosh, A. S. Subbiah, S. K. Sarkar, *J. Phys. Chem. Lett.* **2015**, *6*, 3180.

[12] L. M. Wheeler, D. T. Moore, R. Ihly, N. J. Stanton, E. M. Miller, R. C. Tenent, J. L. Blackburn, N. R. Neale, *Nat. Commun.* **2017**, *8*, 1722.

[13] J. Lin, M. Lai, L. Dou, C. S. Kley, H. Chen, F. Peng, J. Sun, D. Lu, S. A. Hawks, C. Xie, F. Cui, A. P. Alivisatos, D. T. Limmer, P. Yang, *Nat. Mater.* **2018**, *17*, 261.

[14] B. Conings, J. Drijkoningen, N. Gauquelin, A. Babayigit, J. D'Haen, L. D'Olieslaeger, A. Ethirajan, J. Verbeeck, J. Manca, E. Mosconi, F. D. Angelis, H.-G. Boyen, *Adv. Energy Mater.* **2015**, *5*, 1500477.

[15] X.-G. Zhao, D. Yang, J.-C. Ren, Y. Sun, Z. Xiao, L. Zhang, *Joule* **2018**, *2*, 1662.

[16] X.-G. Zhao, J.-H. Yang, Y. Fu, D. Yang, Q. Xu, L. Yu, S.-H. Wei, L. Zhang, *J. Am. Chem. Soc.* **2017**, *139*, 2630.

[17] A. H. Slavney, T. Hu, A. M. Lindenberg, H. I. Karunadasa, *J. Am. Chem. Soc.* **2016**, *138*, 2138.

[18] F. Ji, J. Klarbring, F. Wang, W. Ning, L. Wang, C. Yin, J. S. M. Figueroa, C. K. Christensen, M. Etter, T. Ederth, L. Sun, S. I. Simak, I. A. Abrikosov, F. Gao, *Angew. Chem.* **2020**, *132*, 15303.

[19] J. Luo, X. Wang, S. Li, J. Liu, Y. Guo, G. Niu, L. Yao, Y. Fu, L. Gao, Q. Dong, C. Zhao, M. Leng, F. Ma, W. Liang, L. Wang, S. Jin, J. Han, L. Zhang, J. Etheridge, J. Wang, Y. Yan, E. H. Sargent, J. Tang, *Nature* **2018**, *563*, 541.

[20] F. Ji, G. Boschloo, F. Wang, F. Gao, *Sol. RRL* **2023**, *7*, 202201112.

[21] W. Ning, X. Zhao, J. Klarbring, S. Bai, F. Ji, F. Wang, S. I. Simak, Y. Tao, X. Ren, L. Zhang, W. Huang, I. A. Abrikosov, F. Gao, *Adv. Funct. Mater.* **2019**, *29*, 1807375.

[22] Y. P. Varshni, *Physica* **1967**, *39*, 149.

[23] C. D. Thurmond, *J. Electrochem. Soc.* **1975**, *122*, 1133.

[24] T. T. Tran, J. R. Panella, J. R. Chamorro, J. R. Morey, T. M. McQueen, *Mater. Horiz.* **2017**, *4*, 688.

[25] M. Zacharias, F. Giustino, *Phys. Rev. B* **2016**, *94*, 075125.

[26] A. Francisco-López, B. Charles, O. J. Weber, M. I. Alonso, M. Garriga, M. Campoy-Quiles, M. T. Weller, A. R. Goñi, *J. Phys. Chem. Lett.* **2019**, *10*, 2971.

[27] W. Li, N. U. Rahman, Y. Xian, H. Yin, Y. Bao, Y. Long, S. Yuan, Y. Zhang, Y. Yuan, J. Fan, *J. Semicond.* **2021**, *42*, 072202.

[28] M. Engel, H. Miranda, L. Chaput, A. Togo, C. Verdi, M. Marsman, G. Kresse, *Phys. Rev. B* **2022**, *106*, 094316.

[29] F. Karsai, M. Engel, E. Flage-Larsen, G. Kresse, *New J. Phys.* **2018**, *20*, 123008.

[30] B. Zhang, J. Klarbring, F. Ji, S. I. Simak, I. A. Abrikosov, F. Gao, G. Y. Rudko, W. M. Chen, I. A. Buyanova, *J. Phys. Chem. C* **2023**, *127*, 1908.

[31] V.-A. Ha, G. Volonakis, H. Lee, M. Zacharias, F. Giustino, *J. Phys. Chem. C* **2021**, *125*, 21689.

[32] P. M. M. C. de Melo, J. C. de Abreu, B. Guster, M. Giantomassi, Z. Zanolli, X. Gonze, M. J. Verstraete, arXiv:2207.00364, **2022**.

[33] J. Klarbring, U. Singh, S. I. Simak, I. A. Abrikosov, *Phys. Rev. Mater.* **2023**, *7*, 044605.

[34] G. Greczynski, L. Hultman, *ChemPhysChem* **2017**, *18*, 1507.

[35] G. M. Sheldrick, *SHELX-97, Program for the Refinement of Crystal Structure*, University of Göttingen, Göttingen, Germany **1997**.

[36] P. Kubelka, F. Munk, *Z. Tech. Phys.* **1931**, *12*, 593.

[37] P. E. Blöchl, *Phys. Rev. B* **1994**, *50*, 17953.

[38] G. Kresse, J. Furthmüller, *Comput. Mater. Sci.* **1996**, *6*, 15.

[39] G. Kresse, J. Furthmüller, *Phys. Rev. B* **1996**, *54*, 11169.

[40] G. Kresse, D. Joubert, *Phys. Rev. B* **1999**, *59*, 1758.

[41] J. P. Perdew, A. Ruzsinszky, G. I. Csonka, O. A. Vydrov, G. E. Scuseria, L. A. Constantin, X. Zhou, K. Burke, *Phys. Rev. Lett.* **2008**, *100*, 136406.

[42] S. L. Dudarev, G. A. Botton, S. Y. Savrasov, C. J. Humphreys, A. P. Sutton, *Phys. Rev. B* **1998**, *57*, 1505.

[43] J. Xue, Z. Wang, A. Comstock, Z. Wang, H. H. Y. Sung, I. D. Williams, D. Sun, J. Liu, H. Lu, *Chem. Mater.* **2022**, *34*, 2813.

[44] P. Söderlind, A. Landa, B. Sadigh, *Phys. Rev. B* **2002**, *66*, 205109.

[45] B. Alling, T. Marten, I. A. Abrikosov, *Phys. Rev. B* **2010**, *82*, 184430.

[46] A. Zunger, S.-H. Wei, L. G. Ferreira, J. E. Bernard, *Phys. Rev. Lett.* **1990**, *65*, 353.